

Maximal Overlap Wavelet Statistical Analysis with Application to Atmospheric Turbulence

Charles R. Cornish (ccornish@atmos.washington.edu) and Christopher S. Bretherton

Department of Atmospheric Science, University of Washington, Seattle, WA 98195-1640, USA

Donald B. Percival

Applied Physics Laboratory, University of Washington, Seattle, WA 98195-5640, USA

Abstract. Statistical tools based on the maximal overlap discrete wavelet transform (MODWT) are reviewed, and then applied to a dataset of aircraft observations of the atmospheric boundary layer from the tropical eastern Pacific, which includes quasi-stationary and non-stationary segments. The wavelet methods provide decompositions of variances and covariances, e.g. fluxes, between time scales that effectively describe a broadband process like atmospheric turbulence. Easily understood statistical confidence bounds are discussed and applied to these scale decompositions, and results are compared to Fourier methods for quasi-stationary turbulence. The least asymmetric LA(8) wavelet filter yields coefficients that exhibit better uncorrelatedness across scales than the Haar filter and is better suited for decomposition of broadband turbulent signals. An application to a non-stationary segment of our dataset, namely vertical profiles of the turbulent dissipation rate, highlights the flexibility of wavelet methods.

Keywords: wavelet, marine boundary layer, turbulence, analysis of variance

Abbreviations: ANOVA – Analysis of Variance; DWT – Discrete Wavelet Transform; EDOF – Equivalent Degrees Of Freedom; LA – Least Asymmetric; MODWT – Maximal Overlap Discrete Wavelet Transform; PSD – Power Spectral Density; SST – Sea Surface Temperature

1. Introduction

Geophysical data can be complex in nature. A typical time series of atmospheric turbulence observations can consist of several components. One is a broadband signal at scales smaller than most energetic eddies that conforms to a power law spectral scaling of energy with frequency. Other components often have non-stationary variability at larger scales. If the measurements extend across the boundaries of a turbulent layer, the time series will also include non-turbulent segments.

Various techniques are traditionally used for analyzing such time series. In the time domain, averaging the series using a fixed smoothing window permits the decomposition of a signal into smooth and fluctuating components for successive time segments. In the frequency domain, Fourier analysis is widely used to decompose a series into components at different frequencies. While the former is a localized decomposition in time but not frequency, the latter is a global fit of decomposition by frequency based on the assumption



© 2005 Kluwer Academic Publishers. Printed in the Netherlands.

of stationarity. Both lack the ability to extract localized events occurring over multiple time scales.

Although time windowing and Fourier analysis techniques are widely used for turbulence studies due to their familiarity to practitioners, their specific application may require a priori understanding of the time series and nuances of the particular technique. Applying a windowing technique requires selecting an averaging time long enough to obtain meaningful statistics yet short enough that a slowly varying signal appears stationary. Using Fourier analysis methods may require preprocessing such as mean subtraction, linear or higher order detrending, and data windowing and tapering. The successful application of a particular method depends upon the characteristics of the data under study, which in turn requires the practitioner to make assumptions about the nature of the underlying phenomenon prior to analysis. In this paper we present wavelet techniques as robust alternatives for analyzing intermittent and non-stationary series while requiring minimal user specification of analysis parameters.

In recent years, wavelet analysis has been applied to problems in boundary layer meteorology and other disciplines in geophysics. The orthogonal discrete wavelet transform (DWT) using the Haar wavelet, and a variant known as the Fast Wavelet Transform (FWT), have been introduced by several researchers for boundary layer studies (Katul and Parlange, 1994, Katul and Parlange, 1995 and references within). Analyzing surface-layer turbulent observations via Fourier and FWT power spectra methods, Katul and Parlange (1994) observed that FWT spectra are smoother and better suited for revealing energy scaling laws of atmospheric turbulence, and that the global nature of the Fourier transform distributes energy uniformly across the spectrum whereas the wavelet transform better quantifies the nonuniform distribution of energy. Comparing cospectra computed using Fourier and FWT techniques, Howell and Mahrt (1995) found the decompositions to be qualitatively similar, although the peak Fourier spectra were shifted towards longer wavelengths, which they attributed to differences in averaging lengths between the two techniques. Howell and Mahrt (1995) noted that using a wavelet-based multi-resolution analysis (MRA) decomposition in place of Fourier analysis for examining a quasi-stationary turbulent time series has the advantage of matching the MRA averaging length to the width of a localized event. The resulting wavelet coefficients can be interpreted as scale-dependent zero-mean moving averages and are used to compute a variance associated with each scale.

The DWT is not without its shortcomings, as indicated by several modifications to the FWT method introduced by Howell and Mahrt (1995). First, to relax the power of two restriction on the sample size of the DWT, they added additional sampling points by linear interpolation. While this circumvents the sample size restriction, it does not provide additional meaningful data for

resolving larger scales, and the interpretation of the finest scale fluctuations might be compromised by the interpolation process. Second, they noted that the MRA decomposition via the orthogonal DWT is sensitive to the starting position of the time series and depends on whether a given event resides within or straddles a wavelet averaging window. Howell and Mahrt (1995) also proposed an approach for circumventing the DWT's lack of translation-invariance, but it was fairly complex. They introduced a nonorthogonal cospectrum by computing differences between scales within overlapping windows, which is equivalent to phase shifting or translating a realization of the orthogonal MRA. Finally, they applied maximum oversampling to the nonorthogonal technique to compute cospectra over a continuous range of averaging lengths. In the next section we discuss an alternative nonorthogonal wavelet transform that straightforwardly avoids these DWT shortcomings.

While the Haar filter has been commonly used, other wavelet filters offer alternative statistical properties. Katul and Parlange (1994) analyzed turbulence data using ten Daubechies wavelet filters (Haar plus filter lengths $L = 4, 6, \dots, 20$) and found no significant difference in computed power spectra but did find sensitivity in wavelet statistics to filter selection. We will examine the use of the least asymmetric class of filters to improve wavelet statistics while decreasing sensitivity to filter form and length.

In this paper we present a statistical analysis of atmospheric boundary layer turbulence using an nonorthogonal variant of the discrete wavelet transform. In Section 2 we review the maximal overlap discrete wavelet transform (MODWT) following the concepts and notation in Percival and Walden (2000), and discuss a publicly available comprehensive MODWT software package we have developed. Sections 3 and 4 describe the aircraft atmospheric boundary layer measurements used in this study. Section 5 applies a variety of MODWT-based statistical wavelet analysis methods to our dataset, comparing them to conventional Fourier methods where appropriate. Section 6 presents our conclusions.

2. MODWT Transform

The MODWT is a linear filtering operation that transforms a series into coefficients related to variations over a set of scales. It is similar to the DWT in that both are linear filtering operations producing a set of time-dependent wavelet and scaling coefficients. Both have basis vectors associated with a location t and a unitless scale $\tau_j = 2^{j-1}$ for each decomposition level $j = 1, \dots, J_0$. Both are suitable for analysis of variance (ANOVA) and multi-resolution analysis (MRA).

The MODWT differs from the DWT in that it is a highly redundant, nonorthogonal transform (Percival and Walden, 2000, p. 159). The MODWT

retains downsampled values at each level of the decomposition that would be otherwise discarded by the DWT. The MODWT is well-defined for all sample sizes N , whereas for a complete decomposition of J levels the DWT requires N to be a multiple of 2^J .

The MODWT offers several advantages over the DWT. The redundancy of the MODWT facilitates alignment of the decomposed wavelet and scaling coefficients at each level with the original time series, thus enabling a ready comparison between the series and its decomposition. ANOVAs derived using the MODWT are not influenced by circular shifting of the input time series, whereas values derived using the DWT depend upon the starting point of the series (Percival and Walden, 2000, p. 160). Finally, the redundancy of the MODWT wavelet coefficients modestly increases the effective degrees of freedom (EDOF) on each scale and thus decreases the variance of certain wavelet-based statistical estimates. Since the MODWT is energy conserving, it is well suited for analyzing the scale dependence of variability in ANOVA studies.

Decomposing an infinite sequence $\{X_t\}$ of Gaussian random variables using the MODWT to J_0 levels theoretically involves the application of J_0 pairs of filters. The filtering operation at the j th level consists of applying a wavelet (high-pass) filter $\{\tilde{h}_{j,l}\}$ to yield a set of wavelet coefficients

$$\bar{W}_{j,t} = \sum_{l=0}^{L_j-1} \tilde{h}_{j,l} X_{t-l} \quad (1a)$$

and a scaling (low-pass) filter $\{\tilde{g}_{j,l}\}$ to yield a set of scaling coefficients

$$\bar{V}_{j,t} = \sum_{l=0}^{L_j-1} \tilde{g}_{j,l} X_{t-l} \quad (1b)$$

for all times $t = \dots, -1, 0, 1, \dots$ (Percival and Walden, 2000, p. 169). The equivalent wavelet $\{\tilde{h}_{j,l}\}$ and scaling $\{\tilde{g}_{j,l}\}$ filters for the j th level are a set of scale-dependent localized differencing and averaging operators, respectively, and can be regarded as stretched versions of the base ($j = 1$) filters. The j th level equivalent filter coefficients have a width $L_j = (2^j - 1)(L - 1) + 1$, where L is the width of the $j = 1$ base filter. In practice, the filters for $j > 1$ are not explicitly created because the wavelet and scaling coefficients can be generated sequentially using an elegant algorithm that involves just the $j = 1$ filters operating on the j th level scaling coefficients to generate the $j + 1$ level wavelet and scaling coefficients (Percival and Walden, 2000, p. 174). The j th level wavelet coefficients characterize those components of the signal with fluctuations matching the unitless scale $\tau_j = 2^{j-1}$. If $\{X_t\}$ is either a stationary process or a non-stationary process with stationary backward differences, and L is suitably chosen, then $\bar{W}_{j,t}$ is a Gaussian stationary process with zero-mean and known power spectral density (Percival and Walden, 2000, p. 307).

In addition, MODWT coefficients for different scales are approximately uncorrelated and are hence useful statistical measures for partitioning variability by scale.

Real-world geophysical signals are usually sampled over a finite interval at discrete times. To complete the filtering operation at each level for a finite time series $\{X_t\}, t = 0, \dots, N-1$, the MODWT treats the series as if it were periodic, whereby the unobserved samples $X_{-1}, X_{-2}, \dots, X_{-N}$ are assigned the observed values at $X_{N-1}, X_{N-2}, \dots, X_0$. The MODWT coefficients are thus given by

$$\tilde{W}_{j,t} = \sum_{l=0}^{L_j-1} \tilde{h}_{j,l} X_{t-l \bmod N} \quad (2a)$$

and

$$\tilde{V}_{j,t} = \sum_{l=0}^{L_j-1} \tilde{g}_{j,l} X_{t-l \bmod N} \quad (2b)$$

for $t = 0, \dots, N-1$. This periodic extension of the time series is known as analyzing $\{X_t\}$ using ‘circular boundary conditions’. There are L_j-1 wavelet and scaling coefficients that are influenced by the extension, which we refer to as ‘the boundary coefficients.’ Since L_j increases with j , the number of boundary coefficients increases with scale. Exclusion of boundary coefficients in ANOVA statistics, e.g. the wavelet variance, provides unbiased estimates. The subset of $\tilde{W}_{j,t}$ that are nonboundary coefficients are identical to $\bar{W}_{j,t}$. Inclusion of boundary coefficients can bias certain statistical estimates, but using the boundary coefficients can decrease the mean squared error, as discussed in Section 5.2.2.

Circular boundary conditions can be problematic for nonperiodic signals that display discontinuities between start and end times. The problem can be diminished by applying an appropriate extension to the series and subsequently calculating the MODWT on the extended series. A common extension, which we will adopt, is the use of ‘reflection boundary conditions’ to extend the series to length $2N$; i.e., the unobserved samples $X_{-1}, X_{-2}, \dots, X_{-N}$ are assigned the observed values at X_0, X_1, \dots, X_{N-1} . Formally we define the extended series $\{X'_t\}$ by setting $X'_t = X_t$ for $t = 0, \dots, N-1$ and $X'_t = X_{2N-1-t}$ for $t = N, \dots, 2N-1$. Thus for reflection boundary conditions (2a) and (2b) can be rewritten as

$$\tilde{W}_{j,t} = \sum_{l=0}^{L_j-1} \tilde{h}_{j,l} X'_{t-l \bmod 2N} \quad (3a)$$

and

$$\tilde{V}_{j,t} = \sum_{l=0}^{L_j-1} \tilde{g}_{j,l} X'_{t-l \bmod 2N} \quad (3b)$$

using the extended series $\{X'_t\}$.

2.1. MODWT PARAMETERS

In addition to the selection of appropriate boundary conditions, applying the MODWT to a time series requires specification of a wavelet filter and of the index J_0 for the maximum scale of interest. To make appropriate selections we must take into account the goals of the analysis and time series being analyzed.

2.1.1. Wavelet Filter

We first consider the selection of a wavelet filter. The Daubechies class of wavelets possesses appealing regularity characteristics and produces transforms that are effectively localized differences of adjacent weighted averages (Daubechies, 1992). The least asymmetric (LA) subclass (aka symmlets) has approximate linear phase and exhibits near symmetry about the filter midpoint. This linear phase property means that events and sinusoidal components in the wavelet and scaling coefficients at all levels can be aligned with the original time series. For the MODWT, this alignment is achieved by circularly shifting the coefficients by an amount dictated by the phase delay properties of the basic filter.

LA filters are available in even widths L . The optimal filter width is dependent on the characteristics of the signal and problem domain of interest. A wider filter is smoother in appearance and reduces the possible appearance of artifacts in an MRA due to the filter shape. It also results in better uncorrelatedness between wavelet coefficients across scales for certain time series, which is useful for deriving confidence bounds from certain wavelet-based estimates (Craigmile and Percival, 2005). However, using a wider filter results in many more boundary coefficients, especially at higher levels.

For the present study we select the LA(8) filter since it yields coefficients that are approximately uncorrelated between scales while having a filter width short enough such that the impact of boundary conditions is tolerable. Figure 1 shows the equivalent wavelet $\{\tilde{h}_{j,l}\}$ and scaling $\{\tilde{g}_{j,l}\}$ filter coefficients for the LA(8) filter for the first three levels of decomposition. The coefficients have been translated so that the filter midpoints are aligned. The autocorrelation width for the equivalent scaling filter, $w_{a,j}$ (Percival and Walden, 2000, p. 174), shown as a horizontal line segment below each equivalent filter, is a measure of the effective averaging interval and is equal to 2^j . It can be used to indicate the portion of the time series making the main contribution to the wavelet and scaling coefficients at a particular location. For the LA(8) filter, $L_j/w_{a,j}$ tends towards a value of 7 with increasing j , and the filtering operation is effectively localized to a small region near the center. By contrast, for the Haar filter, since $L_j = w_{a,j}$ for all j , the ratio of equivalent filter width to autocorrelation width is unity for all j . Thus, although the LA(8) filter involves some contribution from a sampling window seven times as wide as

the Haar filter, its output mainly reflects a band of 2^j samples centered on the filtering time, just like the Haar filter.

Figure 2 shows the squared gain functions for the LA(8) (solid curve) wavelet filters for levels 1–3 and the third-level scaling filter as a function of unitless frequency f , and illustrates the band-pass nature of the MODWT. The j th level equivalent filter has a nominal octave pass-band $2^{-(j+1)} < f < 2^{-j}$ of width $w_{b,j} = 2^{-(j+1)} = 1/(2w_{a,j})$. These pass-bands are delineated by the vertical lines in the figure. For reference, the squared gain functions for the Haar ($L = 2$) (dashed curve) and LA(16) (dashed-dotted curve) filters are also plotted in Figure 2. The narrower Haar filter is noticeably less concentrated within the nominal pass-bands than the other two filters. While the wider LA(16) filter is slightly more concentrated in the pass-band than the LA(8) filter, the LA(8) has the practical advantage of having half the width and therefore much fewer boundary coefficients. Thus, for shorter filters (e.g. Haar), the equivalent wavelet filters at the different scales include more leakage from frequencies outside the octave pass-band compared to longer filters. For a broadband process with a power law dependence on scale (such as the inertial subrange of turbulence), this leakage can obscure the true scale dependence for certain power laws of interest.

2.1.2. Number of levels

A time series can be completely or partially decomposed into a number of levels. For complete decomposition of a series of length $N = 2^J$ using the DWT, the maximum number of levels in the decomposition is J . In practice, a partial decomposition of level $J_0 \leq J$ suffices for many applications. A J_0 level DWT decomposition requires that N be an integral multiple of 2^{J_0} . The MODWT can accommodate any sample size N and, in theory, any J_0 . In practice, the largest level is commonly selected such that $J_0 \leq \log_2(N)$ in order to preclude decomposition at scales longer than the total length of the time series. In particular, for alignment of wavelet coefficients with the original series, the condition $L_{J_0} < N$, i.e. the width of the equivalent filter at the J_0 th level is less than the sample size, should be satisfied to prevent multiple wrappings of the time series at level J_0 . Selection of J_0 determines the number of octave bands and thus the number of scales of resolution in the decomposition.

For the current study sample sizes N are $O(10^4)$, and setting $J_0 = 10$ satisfies the $L_{J_0} < N$ restriction. In our presentation of statistical estimators for quasi-stationary turbulence, setting $J_0 = 13$ allows additional scales to be included in the wavelet decomposition while satisfying the less restrictive $J_0 \leq \log_2(N)$ criteria.

2.2. WMTSA TOOLKIT

For the convenience of potential users of MODWT-based statistical analysis, we have developed a WMTSA (Wavelet Methods for Time Series Analysis) toolkit for MATLAB (Cornish et al., 2003) available at

<http://www.atmos.washington.edu/~wmtsa>

which implements the MODWT filters and transform documented in Percival and Walden (2000). The implementation of the MODWT uses a modification of a pyramid algorithm first proposed for the DWT by Mallat (1989). This modification is discussed in detail by Percival and Walden (2000, pp. 174–9). The WMTSA toolkit generated all of the results discussed in this paper.

3. Aircraft Measurements

The dataset used as a case study for our MODWT analysis is an airborne atmospheric turbulence dataset collected during the East Pacific Investigation of Climate (EPIC) 2001 field experiment. Raymond et al. (2004) present an overview of EPIC 2001. One goal of EPIC was to observe the atmospheric boundary layer structure along 95° W northward from the equator into the Pacific Intertropical Convergence Zone (ITCZ) at 10 – 12° N. This region encompasses some of the strongest gradients in sea-surface temperature (SST) in the tropical oceans, between cold upwelled water of 18 – 19° C near the equator and SSTs 10° C warmer in the ITCZ. In boreal fall, strong northward surface winds blow air rapidly across this SST gradient, producing rapid northward changes in boundary layer structure and turbulence. De Szoeke et al. (2005) document the EPIC 95° W turbulence and boundary layer observations; we review the salient details here. The experimental campaign included numerous flights of the instrumented National Center for Atmospheric Research (NCAR) C130 aircraft during September and October of 2001. For the present study, we examine high-resolution (25 Hz) measurements of wind velocity, temperature, and humidity taken during a representative research flight (RF03) flown on September 7, 2001 along a 95° W transect between 14° N and 1° S.

The aircraft flew southward along 95° W at a speed of ~ 100 ms^{-1} in a "sawtooth" pattern, making continuous in-situ observations that can be subdivided into time segments corresponding to legs flown near the sea surface, ascending or descending profiles through the boundary layer, and above the boundary layer (Figure 3). During low legs the aircraft flew near the surface at a nominal altitude of 30 m, and during high legs it flew above the boundary layer level at a nominal altitude of 1600 m. The vertical aircraft speed during the profile legs was ~ 4 m s^{-1} . Each leg lasted ~ 6 min, covering ~ 36 km

horizontal extent during which $O(10^4)$ samples were recorded at a frequency of 25 Hz, corresponding to one sample per four horizontal meters. Our present analysis is limited to examining low and profile legs near the equator (1°S to 3°N), where the boundary layer evolves from a shear-driven to a convective structure.

For our analysis, we extracted subsets of observations encompassing specific flight legs of interest. For profile legs, we used a sufficiently broad segment of the time series such that no wavelet coefficients at times and levels under consideration were influenced by the choice of boundary conditions. For the low legs, we truncated the sample at the leg end points and used reflection boundary conditions to extend the time series. The rationale for these choices is that the series subsets are nearly statistically stationary for level legs but are not for the profile legs. Hence extension of a low leg using data from adjacent profiles would undesirably bias statistical quantities, such as the wavelet variance, averaged over a low leg.

4. Ambient Conditions

The ambient mean-state conditions during flight RF03 are characterized by a large SST gradient of 7°C between 1°S and 2.5°N (Figure 4). At 1°S the near-surface air is slightly warmer than the ocean surface. However, because it flows northward faster than the atmosphere can respond to a warming ocean, the air temperature at 2.5°N is roughly 3°C cooler than the SST. Aircraft profiles show a shallow layer of northward mean flow ($v > 0$) just above the sea surface flowing from the cold to warm SST region (top panels of Figure 5). The virtual potential temperature profiles (bottom panels of Figure 5) show that this high-velocity layer is capped by a strong inversion layer. These SST and air temperature gradients and mean wind profiles were typical of EPIC 2001 (Raymond et al., 2004, De Szoeke et al., 2005).

We now discuss these structures and their relationship to boundary layer turbulence in the two SST regimes in more detail. Over the region of cold SST at 0.5°S , the vertical profile of the northward velocity (top left panel of Figure 5) shows a shear zone between 30 and 200 m near the surface below a jet peaking at 10 m s^{-1} between 300 and 600 m. The virtual potential temperature profile (bottom left panel of Figure 5) shows a slightly stable boundary layer near the surface (30–200 m) above which lies a near-neutral residual layer (300–600 m). A stably stratified inversion layer extends from 600 m to 1200 m. The vertical velocity profile over the cold SST region (middle left pane of Figure 5) suggests turbulence (marked by high-frequency fluctuations) in several distinct layers. Near the sea surface (30–200 m), the turbulent fluctuations are associated with the presence of strong vertical shear in the horizontal flow. Just above the residual layer, turbulence is present within a

thin stratocumulus cloud layer (600–650 m). Above 1300 m, another layer of convective turbulence is evident in both the vertical velocity fluctuations and the nearly adiabatic potential temperature profile. We believe this is driven by strong radiative cooling of air at the top of a moist layer extending about 1600 m. A wave-like structure is present in the velocity profiles of leg 36 in the stably stratified region above the inversion in the range between 700 and 1300 m. The complexity of the vertical structure in this profile makes it particularly attractive for wavelet analysis.

In the region of warmer SST at 1.1°N, the meridional wind and virtual potential temperature profiles (top and bottom center panels of Figure 5) show that the residual layer and northward jet have disappeared and the inversion layer has weakened, while a mixed layer has developed between 30 m and 700 m. The corresponding vertical velocity profile (middle center panel of Figure 5) shows enhanced turbulence from 30 to 700 m associated with convection forced by the underlying warm sea surface. Over the warmest SST at 2.7°N, the velocity and temperature profiles (right panels of Figure 5) show that the convective mixed layer thickens to 850 m while the inversion layer has further weakened.

5. Application of Wavelet Analysis

5.1. WAVELET COEFFICIENTS

Using the MODWT transform (2), we calculate wavelet and scaling coefficients for observations taken during low and profile legs. We select a partial level of decomposition of $J_0 = 10$ to provide an ample number of nonboundary coefficients at the higher levels. Figure 6 shows the resultant decomposition of the vertical velocity for the descent leg 36, corresponding to the profile shown in the left middle panel of Figure 5. The bottom panel of Figure 6 shows the time series of the vertical velocity (jagged solid curve). The aircraft altitude (dotted curve) and the ambient air temperature (smooth dashed curve) are also plotted for reference. The top panel shows the wavelet coefficients $\tilde{W}_{j,t}$ for levels $j = 1-10$ and the \tilde{V}_{10} scaling coefficients plotted on the same vertical scale as the lower panel. Labels to the left indicate the associated physical scale $\tau_j^* = \tau_j U_0 \Delta t = 2^{(j-1)} U_0 \Delta t$, where U_0 is the mean aircraft speed of 100 ms^{-1} and Δt is the sampling period of 0.04 s. Vertical dashed lines across both panels indicate the start and stop points of the aircraft descent. Vertical dotted lines indicate the aircraft altitude at 250 m intervals. For each level (but discernible only for $j \geq 5$) solid vertical lines near the end points demarcate the boundaries outside of which the coefficients are influenced by boundary conditions. The sampled time series for the descent profile leg was extended into adjacent high and low legs so that the coefficients within the

profile leg are influenced more by data in the adjacent legs than by boundary conditions.

The coefficients in Figure 6 have been plotted after circular shifting of the wavelet coefficients $\widetilde{W}_{j,t}$ for alignment with the original time series. The shifted vector is denoted by $T^{-v_j}\widetilde{W}_j$, where v_j indicates the number of time points the coefficients have been shifted. These shifts are a function of the filter class, filter length and level. For LA filters, when $L/2$ is even (as is the case for the LA(8) filter), the shift is expressed as

$$v_j^{(G)} = \frac{(L_j - 1)(L - 2)}{2(L - 1)} \quad (4a)$$

for scaling coefficients, and

$$v_j^{(H)} = -\frac{L_j}{2} \quad (4b)$$

for wavelet coefficients (Percival and Walden, 2000, pp. 112–4). Aligning the coefficients with the original time series allows us to examine co-located events across a range of scales.

The broadband nature of turbulence is evident in the wavelet decomposition. As the aircraft starts its descent profile, the turbulent layers identified in Figure 5 at 1300–1500 m (radiation-driven convection), 600–700 m (cloud), and < 250 m (shear driven) are readily evident in Figure 6 by the similarly enhanced amplitudes of the wavelet coefficients across levels $j = 1$ –6 corresponding to physical scales $\tau_j^* = 4$ –128 m. Between 700 and 1250 m wave-like variations are evident at levels 7, 8 and 9 (corresponding to 256, 512 and 1024 m scales). These are non-turbulent fluctuations, since they do not show the enhanced variability in the wavelet coefficients at smaller scales that one would expect in a turbulent energy cascade. As the aircraft leveled off at ~ 35 m into the adjacent low leg for flight time > 17510 s, it entered a region of quasi-stationary shear-produced turbulence near the surface, which is evident from the enhanced wavelet coefficient amplitudes over level range $j = 1$ –7.

5.2. WAVELET VARIANCE

The decomposition of a time series into scale-dependent coefficients using the MODWT permits the statistical analysis of a signal as a function of scale. The MODWT is energy conserving:

$$\|\mathbf{X}\|^2 = \sum_{j=1}^{J_0} \|\widetilde{\mathbf{W}}_j\|^2 + \|\widetilde{\mathbf{V}}_{J_0}\|^2. \quad (5)$$

From (5) we can derive a scale-dependent ANOVA from the wavelet and scaling coefficients:

$$\hat{\sigma}_X^2 = \|\mathbf{X}\|^2 - \bar{X}^2 = \frac{1}{N} \sum_{j=1}^{J_0} \|\tilde{\mathbf{W}}_j\|^2 + \frac{1}{N} \|\tilde{\mathbf{V}}_{J_0}\|^2 - \bar{X}^2. \quad (6)$$

Considering only the nonboundary coefficients, the wavelet variance $v_X^2(\tau_j)$ is defined as the expected value of $\tilde{W}_{j,t}^2$. The wavelet variance will be time independent only if the time series is stationary or has stationary increments; this can be assumed for the low-level legs but not the profiles. When it is time independent, the true wavelet variance $v_X^2(\tau_j)$ represents the contribution to the (possibly infinite) variance of $\{X_t\}$ at the unitless scale $\tau_j = 2^{j-1}$ and can be estimated by the unbiased estimator

$$\hat{v}_{X,u}^2(\tau_j) = \frac{1}{M_j} \sum_{t=L_j-1}^{N-1} \tilde{W}_{j,t}^2, \quad (7)$$

where $M_j = N - L_j + 1$ is the number of nonboundary coefficients at the j th level.

We also consider a biased estimator of $v_X^2(\tau_j)$ that makes use of reflection boundary conditions and includes all $2N$ wavelet coefficients resulting from applying the MODWT to the reflected series $\{X'_t\}$. The biased estimator takes the form

$$\hat{v}_{X,b}^2(\tau_j) = \frac{1}{2N} \sum_{t=0}^{2N-1} \tilde{W}_{j,t}^2. \quad (8)$$

Under appropriate conditions, the large scale sample distributions of both estimators take analogous forms and can be used to establish confidence intervals for the true wavelet variance. Recent work by Aldrich (2005) indicates that $\hat{v}_{X,b}^2(\tau_j)$ has a significantly smaller mean-squared error than $\hat{v}_{X,u}^2(\tau_j)$ for small sample sizes, but the two estimators become indistinguishable as N becomes large. This theory lends to an approximation to the distribution of both estimators in terms of a scaled χ^2 distribution with η_j equivalent degrees of freedom (EDOF), which accounts for correlation between the $\tilde{W}_{j,t}$. Percival and Walden (2000, pp. 313–5) present several methods for calculating η_j . The simplest but somewhat conservative method is to set

$$\eta_j = \max\{\tilde{N}_j/2^j, 1\}. \quad (9)$$

where $\tilde{N}_j = M_j$ for the unbiased estimator, and $\tilde{N}_j = N$ for the biased estimator. Using these EDOFs, $(1 - 2p) \times 100\%$ confidence intervals for $v_X^2(\tau_j)$ can be approximated by

$$\left[\frac{\eta_j \hat{v}_X^2(\tau_j)}{Q_{\eta_j}(1-p)}, \frac{\eta_j \hat{v}_X^2(\tau_j)}{Q_{\eta_j}(p)} \right], \quad (10)$$

where $\hat{v}_X^2(\tau_j)$ stands for either $\hat{v}_{X,u}^2(\tau_j)$ or $\hat{v}_{X,b}^2(\tau_j)$, and $Q_{\eta_j}(p)$ is the $p \times 100\%$ percentage point for the χ^2 distribution with η_j EDOF (Percival and Walden, 2000, p. 313). While this conservative method for calculating the EDOF yields the same value for η_j for both the MODWT and DWT, the MODWT actually provides a slightly better estimate of $v_X^2(\tau_j)$, with a variance that can be up to a factor of two smaller than that of the DWT-based estimator. A more complicated method for calculating the EDOF that is asymptotically correct as $N \rightarrow \infty$ is described by Percival and Walden (2000, p. 313). In the following analysis we stick with the simple formula (9), and set $p = 0.025$ to establish 95% confidence intervals.

5.2.1. Filter comparison of wavelet variance estimates

Figure 7 shows the resulting unbiased estimates and confidence intervals for the wavelet variance using the LA(8) (solid curve) and Haar (dotted curve) filters for the vertical velocity observations of low leg 32, in a rapidly developing convective boundary layer about 500 m deep in the region of rapid northward SST rise. For reference we have plotted a line on Figure 7 with a slope of $2/3$ for levels $j = 2-6$, which represents the expected shape of the variance curve within the inertial subrange for isotropic turbulence, assuming a perfect octave bandpass filter. Labeled below the horizontal axis are the physical scales τ_j^* in meters associated with the non-dimensional levels. Assuming Taylor's frozen turbulence hypothesis to be valid as the aircraft transverses through the atmosphere, we can associate observed temporal fluctuations to spatial variations. Using a nominal aircraft speed of $U_0 = 100 \text{ m s}^{-1}$ and sampling period Δt of 0.04 s, the smallest level ($j = 1$) corresponds to a spatial scale $\tau_1^* = U_0 \Delta t = 4 \text{ m}$ and the largest level ($j = 10$) corresponds to $\tau_{10}^* = 2^{10-1} \times 4 \text{ m} = 2048 \text{ m}$. For leg 32 ($N = 12575$), the $M_j = N - L_j - 1 > 0$ restriction at all levels dictates the maximum level of wavelet variance decomposition for the unbiased estimator to be $J_0 = 10$.

Both curves in Figure 7 show general agreement in form and peak at level 6 corresponding to a scale of 128 m, which is about one-quarter of the mixed layer depth. While the confidence intervals overlap for levels 5 and higher, the curves and their confidence intervals diverge for $j < 5$. Compared to the LA(8), the Haar wavelet variance estimates are systematically larger at the smaller scales and have a flatter slope in the inertial subrange levels. As seen in Figure 2, the Haar filter is less perfect than the LA(8) as an octave band filter and yields a scale-dependent variance that suffers from energy leakage at smaller scales. The drop in the wavelet variance at level $j = 1$ below the linear trend for the level range $j = 2$ to 6 is due to a drop-off in instrument sensitivity above 10 Hz and low-pass filtering prior to recording the data.

5.2.2. Biased wavelet variance estimates

The unbiased estimator of the wavelet variance includes only contributions from $N - L_j + 1$ nonboundary coefficients, and is restricted to levels where $L_j - 1 < N$, i.e. $J_0 = \log_2(N/(L - 1) - 1)$. The biased estimator can be computed for any level as it uses all N coefficients at all scales. However to obtain statistically significant results, we need to limit J_0 to a level where at least some of the wavelet coefficients are not heavily influenced by the boundary conditions.

The calculation of a MODWT wavelet coefficient for a given time t and level j is the convolution of the equivalent wavelet filter with L_j adjacent time points centered at t . However, most of the contribution to this coefficient comes from the adjacent times within a half autocorrelation width, i.e., the $w_{a,j}$ time points centered at t . Recognizing this, we restrict J_0 to a level that includes at least some boundary wavelet coefficients that are weakly influenced by contributions by the series end points. Quantitatively we require $N - w_{a,j} + 1 > 0$ weakly influenced wavelet coefficients. Since for the Haar filter $L_j = w_{a,j}$ for all j , this constraint is equivalent to selecting the maximum level for the unbiased estimator for the Haar for a given sample size. Setting $J_0 = \log_2(N)$ satisfies this requirement. For the present study, using the biased estimator allows us to extend the wavelet variance to larger scales from $J_0 = 10$ to $J_0 = 13$ for time series of length $N = O(10^4)$.

A comparison of the two wavelet variance estimators using the LA(8) filter is shown in Figure 8 for low leg 32. The wavelet variance estimates for both estimators agree well for all scales except for $j = 10$, for which the unbiased estimate is lower than the biased. The confidence bounds of the unbiased estimator (solid lines) become noticeably wider than those for the biased estimator (dotted lines) as j increases. For the leg 32 data series, the maximum level of decomposition for the unbiased estimator is $J = 10$, while the less restrictive biased estimator allows decomposition to $J = 13$. For $j = 11-13$, a minimum in the biased wavelet variance estimate occurs at $j = 12$, but note that the confidence intervals broaden with greater uncertainty at these scales.

Using the biased estimator, we calculate the wavelet variance of the vertical velocity and virtual potential temperature for three low legs at latitudes spanning the region of transition from cold to warm SST. Figure 9 shows the wavelet variance (solid curves) and 95% confidence intervals (dotted curves) for levels $j = 1-13$ corresponding to spatial scales $\tau_j^* = 4-16384$ m. The confidence bounds computed using (10) widen with level as the EDOFs decrease with scale. We can readily identify localized maxima in the wavelet variances at smaller scales ($j \approx 5-7$) due to turbulent fluctuations, enhanced variability at larger scales ($j = 11-13$) due to mesoscale circulations, and a gap between the two where energy sources are absent. Using the biased estimator to extend J_0 to 13 allows us to observe the ‘mesoscale gap’ in variability in Figure 9 that

was not readily apparent in Figure 7 because the unbiased estimator cannot be computed for levels $j > 10$.

Over the region of cold SST at -0.82°S (leg 37), the peak in wavelet variance at small scales for the vertical velocity occurs at level 5, corresponding to a scale of 64 m, while that for the virtual potential temperature peaks at level 3. Northward over the regions of warmer SST (legs 32 and 27), the peak in the wavelet variance at small scales for the vertical velocity shifts towards level 7, corresponding to a scale of 256 m, and the peak magnitude of the wavelet variance increases by a factor of 5. The wavelet variance of the virtual potential temperature shows a similar shift in its peak towards larger scales, while its magnitude is enhanced by a factor of 10. These vertical velocity variance results are consistent with other observations of enhanced variance at scales of hundreds of meters for convective conditions compared to neutrally stratified conditions (Grossman, 1982) and a large increase in the the variance in the transition from cold to warm waters across a SST front (Kwon et al., 1998).

5.3. COMPARISON OF WAVELET TO FOURIER POWER SPECTRUM

The MODWT transform is an approximate octave-band decomposition with each band corresponding to a particular scale. The j th level wavelet variance is approximately equal to twice the integral of the power spectral density (PSD), $S_X(f)$, over the corresponding octave band:

$$v_X^2(\tau_j) \approx 2 \int_{1/(2^{j+1}\Delta t)}^{1/(2^j\Delta t)} S_X(f) df. \quad (11)$$

The factor of 2 arises because $S_X(f)$ is two-sided and symmetric about zero. Recall that the average value of a function F over the interval (a, b) is defined as

$$\frac{1}{b-a} \int_a^b F(x) dx. \quad (12)$$

Let C_j be the average value of $S_X(f)$ over the interval $\frac{1}{2^{j+1}\Delta t} < f \leq \frac{1}{2^j\Delta t}$:

$$C_j = 2^{j+1}\Delta t \int_{1/(2^{j+1}\Delta t)}^{1/(2^j\Delta t)} S_X(f) df. \quad (13)$$

From (11) and (13) we can define an estimator of the average PSD in the j th octave band from the wavelet variance;

$$\hat{C}_j = 2^j \hat{v}_X^2(\tau_j) \Delta t. \quad (14)$$

From (10) and (14), we can obtain a confidence interval for C_j

$$\left[\frac{2^j \eta_j \hat{v}_X^2(\tau_j) \Delta t}{Q_{\eta_j}(1-p)}, \frac{2^j \eta_j \hat{v}_X^2(\tau_j) \Delta t}{Q_{\eta_j}(p)} \right], \quad (15)$$

using the EDOF η_j defined in (9).

Using (14), we estimate the band-average PSD using the LA(8) filter for the vertical velocity time series of low leg 32. For comparison we also compute an estimate of the PSD using a Fourier multitaper window method with 7 data tapers (Percival and Walden, 1993, Chapter 7). The results are plotted in Figure 10 using a factor of 10 offset between spectra. Also plotted for comparison is a line with $-5/3$ slope illustrating the expected slope of spectra conforming to a Kolmogorov power law for isotropic turbulence in the inertial subrange. The octave-band average wavelet power spectrum is plotted at the geometric center of the band using an ‘*’. The height of surrounding boxes indicates the 95% confidence interval for C_j , and the width indicates the nominal octave-band.

The wavelet and multitaper power spectra curves of Figure 10 agree well with a $-5/3$ slope power law for $f > 0.5$ Hz, which corresponds to wavelet level $j = 6$ and a physical scale of 128m. Both flatten at the lower frequencies below the inertial subrange. The major difference between the two methods is the degree of variability in the resultant spectra. The multitaper method, like other unsmoothed Fourier power spectral estimates, exhibits considerable variability between adjacent frequencies. The octave-averaging of the wavelet variance estimate greatly reduces variability, especially at high frequencies, giving a very accurate PSD estimate for a broad-band process.

One can achieve the same octave-band averaging effect of the wavelet variance from power spectral estimates by integrating and plotting the power spectral density from highest to lowest frequencies, which yields an ogive curve. A wavelet-based equivalent to an ogive curve can be obtained by plotting

$$\hat{O}_m = \sum_{j=1}^m \hat{v}_X^2(\tau_j) \quad (16)$$

vs. $f_m = (2^{m+1}\Delta t)^{-1}$, where \hat{O}_m and f_m are, respectively, the cumulative sum of wavelet variances and the frequency at the lower limit of the octave band for $\hat{v}_X^2(\tau_m)$. An advantage of the wavelet-based ogive estimator is that we can estimate confidence intervals for it, as follows. If the wavelet spectral estimates are approximately uncorrelated between scales, the random variable \hat{O}_m has approximately a χ^2 distribution with EDOF ζ_m given by

$$\zeta_m = \frac{\left(\sum_{j=1}^m v_X^2(\tau_j) \right)^2}{\sum_{j=1}^m v_X^4(\tau_j)/\eta_j} \quad (17)$$

By using estimates for $v_X^2(\tau_j)$ in the above to form an estimate $\hat{\zeta}_m$ for ζ_m , we obtain an approximate confidence interval for O_m using

$$\left[\frac{\hat{\zeta}_m \hat{O}_m}{Q_{\hat{\zeta}_m}(1-p)}, \frac{\hat{\zeta}_m \hat{O}_m}{Q_{\hat{\zeta}_m}(p)} \right]. \quad (18)$$

Figure 11 shows the ogive curves corresponding to the PSD estimates for the wavelet and multitaper methods of Figure 10 (asterisks and solid curve, respectively). The two curves are in agreement and converge at the lowest frequency to a value close to the sample variance of the original time series. The confidence intervals of the ogive derived via the wavelet method (dashed curves) become wider as j increases (frequency decreases) due to the increased uncertainty in the wavelet variance estimates at large scales.

The confidence intervals for the wavelet-based spectral estimates follow directly from the statistical properties of the wavelet variance, which take into account the covariance structure of the MODWT wavelet coefficients within a given octave band. Corresponding confidence intervals for the multitaper-based octave-band estimates are more difficult to obtain because we would need to determine some sort of model for the structure of the PSD within the octave-band. A crude approximation would be to assume that the PSD is locally flat, but this approach is not particularly appealing for spectra like those conforming to a Kolmogorov power law.

The wavelet and multitaper methods for power spectral estimation yield the same basic information for time series that are well modeled locally in frequency or scale by a power law. The wavelet method offers the advantages of straightforward estimation of the power spectrum and confidence intervals. By contrast, the multitaper and other Fourier methods require the practitioner to deal explicitly with detrending, windowing, data tapers and averaging procedures to reduce bias and variability. On the other hand, for a process with narrow spectral peaks, the enhanced spectral resolution of Fourier power spectral methods makes them clearly preferable over octave-averaging wavelet methods.

5.4. WAVELET COVARIANCE

The wavelet covariance is a measure of the degree of simultaneous correlation between two sets of observations (X and Y) as a function of scale. Including only the nonboundary wavelet coefficients and again assuming time independence, the true wavelet covariance $v_{XY}(\tau_j)$ is defined as the expected value of $\tilde{W}_{X,j,t} \tilde{W}_{Y,j,t}$, and an unbiased estimator for it is given by

$$\hat{v}_{XY}(\tau_j) = \frac{1}{M_j} \sum_{t=L_j-1}^{N-1} \tilde{W}_{X,j,t} \tilde{W}_{Y,j,t}. \quad (19)$$

As was true for the wavelet variance, we can form a biased covariance estimator using the obvious analog of Equation (7). To simplify our discussion, we concentrate on just the unbiased estimator of the wavelet covariance in what follows.

A method for calculating confidence intervals for the true covariance at the j th level based upon the wavelet covariance estimate and a Gaussian assumption is presented by Whitcher et al. (2000) and described here briefly. The unbiased estimator of the auto-covariance sequence for the MODWT coefficients $\tilde{W}_{X,j,t}$ of the series $\{X_t\}$ at the j th level and the lag τ is defined as

$$\hat{s}_{X,j,\tau} = \frac{1}{M_j} \sum_{t=L_j-1}^{N-|\tau|-1} \tilde{W}_{X,j,t} \tilde{W}_{X,j,t+|\tau|}. \quad (20)$$

A similar estimator is defined for the MODWT coefficients of the series $\{Y_t\}$. The cross-covariance sequence of the MODWT coefficients for the X and Y series at the j level is defined as

$$\hat{s}_{XY,j,\tau} = \frac{1}{M_j} \sum_t \tilde{W}_{X,j,t} \tilde{W}_{Y,j,t+\tau}, \quad (21)$$

where the summation is over $t = L_j - 1, \dots, N - \tau - 1$ for $\tau \geq 0$ and over $t = L_j - \tau - 1, \dots, N - 1$ for $\tau < 0$. Whitcher et al. (2000) show that $\tilde{v}_{XY}(\tau_j)$ is asymptotically Gaussian distributed, allowing us to construct an approximate confidence interval for the true wavelet covariance via

$$\left[\hat{v}_{XY}(\tau_j) - \Phi^{-1}(1-p) \frac{\hat{\sigma}_{XY,j}}{\sqrt{M_j}}, \hat{v}_{XY}(\tau_j) + \Phi^{-1}(1-p) \frac{\hat{\sigma}_{XY,j}}{\sqrt{M_j}} \right], \quad (22)$$

where $\Phi^{-1}(1-p)$ is the $p \times 100\%$ percentage point for the standard Gaussian distribution, and

$$\hat{\sigma}_{XY,j}^2 = \frac{\hat{s}_{X,j,0} \hat{s}_{Y,j,0}}{2} + \sum_{\tau=1}^{M_j-1} \hat{s}_{X,j,\tau} \hat{s}_{Y,j,\tau} + \frac{1}{2} \sum_{\tau=-(M_j-1)}^{M_j-1} \hat{s}_{XY,j,\tau}^2. \quad (23)$$

Expressions for the wavelet covariance and confidence intervals using the biased estimator are readily derived by substituting $\tilde{N}_j = N$ for M_j in (22) and by making appropriate adjustments to (19–21) and (23).

Figure 12 shows the biased wavelet covariance estimates with 95% confidence bounds ($p = 0.025$) between the vertical velocity and virtual potential temperature for three low legs. At 0.82°S in the region of cold SST the wavelet covariance is near zero for all scales. North of the equator the wavelet covariance is nonzero and increases in magnitude and level with increasing latitude. It has a peak at level 7 (scale = 256 m) for leg 27. Positive values

of the wavelet covariance indicate buoyancy flux due to convection-driven turbulence near the sea surface.

Cumulative cospectrum or ogive curves provide a ready comparison of wavelet covariance and Fourier cospectra methods. In analogy to Equation (16), the ogive estimator for the cumulative wavelet covariance is given by

$$\hat{O}_{XY,m} = \sum_{j=1}^m \hat{v}_{XY}(\tau_j). \quad (24)$$

Assuming that $\hat{v}_{XY}(\tau_j)$ and $\hat{v}_{XY}(\tau_{j'})$ are independent when $j \neq j'$, the variance of the ogive estimator is

$$\text{var}\{\hat{O}_{XY,m}\} = \sum_{j=1}^m \text{var}\{\hat{v}_{XY}(\tau_j)\}. \quad (25)$$

If $\hat{O}_{XY,m}$ is approximately normally distributed with a mean $O_{XY,m}$ and a variance $\text{var}\{\hat{O}_{XY,m}\}$, we can establish an approximate confidence interval for $O_{XY,m}$ using:

$$\left[\hat{O}_{XY,m} - \Phi^{-1}(1-p) (\text{var}\{\hat{O}_{XY,m}\})^{1/2}, \hat{O}_{XY,m} + \Phi^{-1}(1-p) (\text{var}\{\hat{O}_{XY,m}\})^{1/2} \right]. \quad (26)$$

Setting $p = 0.025$ for 95% confidence bounds, we calculate the ogive estimate using the vertical velocity and virtual potential temperature data of low leg 32 with multitaper and wavelet covariance methods (Figure 13). While both methods yield the same information, the wavelet method is more amenable for providing confidence bounds. Based on the wavelet method, one can read off from Figure 13 that $\overline{w'\theta'_v} = 0.027 \pm 0.003 \text{ K m s}^{-1}$, with essentially all the flux coming from levels $j \leq 11$ (physical scales less than 4 km).

5.5. ENERGY DISSIPATION RATE PROFILES

The magnitude of the variability in the velocity field is an indicator of the intensity of turbulence. For scales within the inertial subrange, kinetic energy present in wavelet coefficients is dissipated by a cascade of turbulent energy from larger to smaller scales. The typical squared magnitude of the wavelet coefficients $\tilde{W}_{j,t}^2$ at small scales allows the examination of variability in kinetic energy dissipation as a function of location in a non-stationary time series. For our example, level 2 rather than level 1 wavelet coefficients are used since the latter are damped by the finite instrument response time and low pass filter preprocessing.

Figure 14 shows profiles of the squared wavelet coefficients for the vertical velocity for legs 36 and 34. Individual points are the square of the level 2

wavelet coefficients and are indicators of the instantaneous turbulent energy at the 8 m scale as observed by the aircraft. For leg 36, boundary layer turbulence is confined to the lowest 300 m associated with the shear zone. Within the boundary layer of leg 34 (altitude < 1000 m), small-scale turbulence is highly variable, with an overall magnitude slowly decreasing with altitude. In both profiles, above the boundary layer turbulence drops off rapidly and is minimal except in isolated layers.

To estimate the true wavelet variance profile sampled in each leg, we calculate the running wavelet variance profiles, which are running averages of the squared wavelet coefficients at fixed height increments. The solid lines shown in Figure 14 are a 400-point running averages corresponding to a level 2 running wavelet variance over 64 m height intervals at 16 m increments. Over the cold SST region (leg 36) shown in the left panel, the running wavelet variance highlights turbulent activity, which is confined to a few discrete layers. Below 200 m is the shear-produced boundary layer. The previously identified turbulent cloud layers at 600 m and above 1350 m are evident as well. Over the warm SST region (leg 34, right panel of Figure 14), the 400-point running wavelet variance (solid line) indicates a 1 km deep turbulent layer.

The 64 m running wavelet variance is still somewhat erratic below 600 m, suggesting a more stable estimate can be obtained by using a longer running average. The dot-dashed line of Figure 14 shows a 1600-point running average corresponding to a running wavelet variance over a height range 256 m at 16 m increments. The 256 m running wavelet variance drops off monotonically with height as one might anticipate for turbulence driven mainly by surface fluxes. For this deeper boundary layer, the 256 m averaging interval appears to be a good compromise, supplying a statistically stable estimate while being short enough to adequately resolve the variance profile. In general, the best choice of average interval will depend on the depth of the turbulence layer and the rate at which it is profiled. During an averaging interval, one should sample across several large eddies to get a reliable variance estimate. The scale of the largest eddies is roughly 1.5 times the depth of the boundary layer (Kaimal et al., 1976). A 1600-point sample spans a 6.4 km horizontal range, which is over four times the estimated large-eddy scale, and thus is arguably sufficient for stably estimating the wavelet variance profile in this case.

Combining our profiles of running wavelet variance of vertical velocity, our previous discussion on the relation between wavelet variance and the octave-band averaged power spectrum, and turbulence theory, wavelet methods provide a convenient and accurate estimate of profiles of local turbulent kinetic energy dissipation ϵ , another useful measure of turbulence intensity. According to Kolmogorov's similarity theory of turbulence, an inertial subrange of wavenumbers exists between energy-containing and dissipation

scales, and contains eddies whose average energy depends only of the rate of viscous dissipation. Within the inertial subrange the one-dimensional power spectrum for velocity components is given by

$$S(k) = c\alpha\varepsilon^{2/3}k^{-5/3}, \quad (27)$$

where α is the Kolmogorov constant ≈ 0.6 , ε is the rate of viscous dissipation of energy, and the constant c has a value of 1 for the longitudinal velocity component and a value of $4/3$ for the transverse and vertical velocity components measured with respect to the aircraft's frame of reference (Garratt, 1992, p. 71). Noting that velocity fluctuations are observed from the aircraft moving through the boundary layer at a speed $U_0 = 100 \text{ m s}^{-1}$, and using Taylor's hypothesis

$$fS(f) = kS(k), \quad (28)$$

where $k = 2\pi f/U_0$, we can express (27) as a velocity frequency spectrum

$$S(f) = c\alpha\left(\frac{2\pi}{U_0}\right)^{2/3}\varepsilon^{2/3}f^{-5/3}. \quad (29)$$

Substituting the estimate (14) of the band-averaged PSD for $S(f)$ into (29) and solving for ε yields an estimate of the energy dissipation rate, namely,

$$\hat{\varepsilon} = \frac{2\pi \hat{C}_j^{3/2} f_c^{5/2}}{U_0 (c\alpha)^{3/2}}. \quad (30)$$

where $f_c = (2^{j+1/2}\Delta t)^{-1}$ is the geometric mean of the frequency f over of the j th octave band. Confidence levels for ε can be established from the confidence levels for C_j . Since the velocity frequency spectrum within the inertial subrange depends on the energy dissipation rate, the estimate for ε should be similar in magnitude across levels corresponding to the inertial subrange. As previously noted the $j = 1$ wavelet variances are impacted by instrumental biases, so we select the $j = 2$ level values of \hat{C}_j for estimating ε .

Figure 15 shows profiles of the energy dissipation profiles for legs 36 and 34 using the results of the 256 m running wavelet variance shown in Figure 14. Error bars indicating the 95% confidence interval are derived from wavelet variance statistics for each 1600-point interval. Over the cold SST region (leg 36) turbulent energy dissipation in the boundary layer is strongest in the lowest 200 m where shear production is strongest. Interestingly, the values for ε are as strong in the layer of radiatively-driven free tropospheric turbulence at the top of the profile as in the shear-layer near the surface. Over the warm SST region (leg 34), the energy dissipation rate shows a 7–10 fold increase compared to leg 36 near the surface due to buoyancy-driven turbulence, and drops monotonically to zero at the top of the boundary layer. Other measurements of the marine boundary layer (R  chou et al., 1995) indicate

that ε above the mixed layer is constant for stable conditions but continues to drop off for convective conditions in agreement with our observations.

5.6. ENERGY BALANCE: ENERGY DISSIPATION VS. BUOYANCY FLUX IN SURFACE LAYER

The overall kinetic energy budget of a turbulent boundary layer is a balance between (1) buoyancy and shear generation of turbulent energy and (2) sinks of turbulent energy dissipation. As a final application of wavelet statistics, we compare buoyancy production and turbulent eddy dissipation in the low legs over the cold and warm SST regions.

The kinematic buoyancy flux is defined as

$$B = \frac{g}{\theta_v} \overline{w' \theta'_v} \quad (31)$$

(Stull, 1988, p. 118). We calculate B directly from the summation over all levels of the wavelet covariance between θ'_v and w' . Figure 16 shows the computed buoyancy flux ('*' in both panels) for low legs 37, 32, and 27. Error bars indicate the 95% confidence intervals.

We calculate turbulent energy dissipation for each of the low legs via the method described in Section 5.5 using the level 2 and level 4 wavelet variances. The left panel of Figure 16 shows the leg-mean energy dissipation rates calculated from the level 2 wavelet variance. The displayed energy dissipation rates $\varepsilon_u, \varepsilon_v, \varepsilon_w$ are, respectively, calculated for the longitudinal, transverse and vertical components of the observed velocity field in the aircraft reference frame. The transverse and vertical estimates of ε are comparable in magnitude, but the longitudinal component (which is in the direction of the aircraft motion) is enhanced by a factor of 2–3. A potential source for this discrepancy is noise in the air pressure measurement system used to sense the winds. For comparison, the right panel of Figure 16 shows the estimates of ε using the level 4 wavelet variance. Comparing the level 2 and 4 estimates, ε derived using the transverse and vertical velocity components are comparable in magnitude, which is expected for the dissipation of turbulent kinetic energy within the inertial subrange. However, estimates of ε_u derived from the level 4 wavelet variance of longitudinal velocity component are less than half of the level 2 estimates, yet 50% larger than the level 4 estimates of ε_v and ε_w . Noting that the air motions in the longitudinal aircraft direction are measured with a slightly different pressure sensing system than the transverse wind components, the change in variability of the longitudinal estimates of ε as a function of scale suggests the presence of instrumental noise.

Over the region of cold SST (0.5°S), the buoyancy flux is much less than the corresponding energy dissipation, as expected in a nearly neutrally stratified, shear-driven boundary layer. Over regions of warm SST ($> 0.5^\circ\text{N}$), the

buoyancy flux at the surface B_S is large. For a dry convective mixed layer of depth H with a linear buoyancy flux profile $B(z) = B_S(1 - 1.2z/H)$ (Stull, 1988, p. 349), the energy dissipation is observed to be fairly constant above the surface layer, with magnitude $\epsilon \approx H^{-1} \int_0^H B(z) dz = 0.4B_S$. At 30 m, the aircraft is not quite above the surface layer, but one still might expect $0.4 B_S$ to be a good predictor of ϵ . Estimates of ϵ_v and ϵ_w are somewhat smaller by 30–50% than this prediction. The estimates of ϵ_u , while closer to predicted values, are suspect due to instrumental noise. Despite considerable effort, we do not yet understand this discrepancy.

6. Conclusions

Using a challenging boundary layer turbulence dataset that is typical of those encountered in geophysics, wavelet-based methods are demonstrated to be an attractive alternative to traditional Fourier-based methods for analysis of broadband and non-stationary time series. While almost any wavelet-based method can be mimicked by a cleverly constructed Fourier method, the wavelet approach invokes fewer user choices and provides confidence bounds on many commonly estimated quantities such as second-order moments. A publicly available toolkit for MATLAB developed by the authors is designed to help popularize wavelet methods for time series analysis by providing a powerful yet simple to use set of functions. The functions as implemented in the toolkit have input parameter (e.g., filter, J_0 , boundary conditions, estimators, etc.) defaults set to reasonable values, allowing the novice user to get started and the experienced user complete control. We plan future work on the development of wavelet methods and enhancements to the toolkit, including multidimensional transforms for application to meteorological and geophysical datasets.

Acknowledgements

This research was supported by the National Science Foundation under Grant No. DMS 0222115. Any opinions, findings, and conclusions or recommendations expressed in this material are those of the author(s) and do not necessarily reflect the views of the National Science Foundation.

References

Aldrich, E.: 2005, 'Alternative Estimators for Wavelet Variance'. Master's thesis, Department of Statistics, University of Washington, Seattle, WA.

- Cornish, C. R., D. B. Percival, and C. S. Bretherton: 2003, 'The WMTSA wavelet toolkit for data analysis in the geosciences'. *Eos Trans. AGU* **84**(46). Fall Meet. Suppl., Abstract NG11A-0173.
- Craigmile, P. F. and D. B. Percival: 2005, 'Asymptotic Decorrelation of Between-Scale Wavelet Coefficients'. *IEEE Transactions on Information Theory* **51**(3), 1039–1048.
- Daubechies, I.: 1992, *Ten Lectures on Wavelets*. Philadelphia: SIAM.
- De Szoeko, S. P., C. S. Bretherton, N. A. Bond, M. F. Cronin, and B. Morley: 2005, 'EPIC 95°W Observations of the Eastern Pacific Atmospheric Boundary Layer from the Cold Tongue to the ITCZ'. *J. Atmos. Sci.* **62**(2), 426–442.
- Garratt, J. R.: 1992, *The Atmospheric Boundary Layer*. Cambridge: Cambridge University Press.
- Grossman, R. L.: 1982, 'An analysis of vertical velocity spectra obtained in the BOMEX fair-weather, trade-wind boundary layer'. *Boundary-Layer Meteorol.* **23**, 323–357.
- Howell, J. F. and L. Mahrt: 1995, 'Multiresolution flux decomposition'. *Boundary-Layer Meteorol.* **83**, 117–137.
- Kaimal, J. C., J. C. Wyngaard, D. A. Haugen, O. R. Coté, Y. Izumi, S. J. Caughey, and C. J. Readings: 1976, 'Turbulent structure in the convective boundary layer'. *J. Atmos. Sci.* **33**, 2152–2169.
- Katul, G. G. and M. B. Parlange: 1994, 'On the active role of temperature in surface-layer turbulence'. *J. Atmos. Sci.* **51**(15), 2181–2195.
- Katul, G. G. and M. B. Parlange: 1995, 'The spatial structure of turbulence at production wavenumbers using orthonormal wavelets'. *Boundary-Layer Meteorol.* **75**(1-2), 81–108.
- Kwon, B. H., B. Bénéch, B. Lambert, P. Durand, A. Druilhet, H. Giordani, and S. Planton: 1998, 'Structure of the marine atmospheric boundary layer over an oceanic thermal front: SEMAPHORE experiment'. *J. Geophys. Res.* **103**(C11), 25,159–25,180.
- Mallat, S. G.: 1989, 'A Theory for Multiresolution Signal Decomposition: The Wavelet Representation'. *IEEE Trans. Pattern Anal. and Machine Intell.* **11**, 674–93.
- Percival, D. B. and A. T. Walden: 1993, *Spectral Analysis for Physical Applications: Multitaper and Conventional Univariate Techniques*. Cambridge: Cambridge University Press.
- Percival, D. B. and A. T. Walden: 2000, *Wavelet Methods for Time Series Analysis*. Cambridge: Cambridge University Press.
- Raymond, D. J., S. K. Esbensen, C. Paulson, M. Gregg, C. S. Bretherton, W. A. Petersen, R. Cifelli, L. K. Shay, C. Ohlmann, and P. Zuidema: 2004, 'EPIC2001 and the coupled ocean-atmosphere system of the tropical East Pacific'. *Bull. Amer. Meteor. Soc.* **85**(9), 1341–1354.
- Réchou, P. Durand, A. Druilhet, and B. Bénéch: 1995, 'Turbulence structure of the boundary layer below marine clouds in the SOFIA experiment'. *Ann. Geophysicae* **13**, 1075–1086.
- Stull, R. B.: 1988, *An Introduction to Boundary Layer Meteorology*. Dordrecht: Kluwer Academic Publishers.
- Whitcher, B. J., P. Guthorp, and D. B. Percival: 2000, 'Wavelet analysis of covariance with application to atmospheric time series'. *J. Geophys. Res.* **105**(D11), 14,941–14,962.

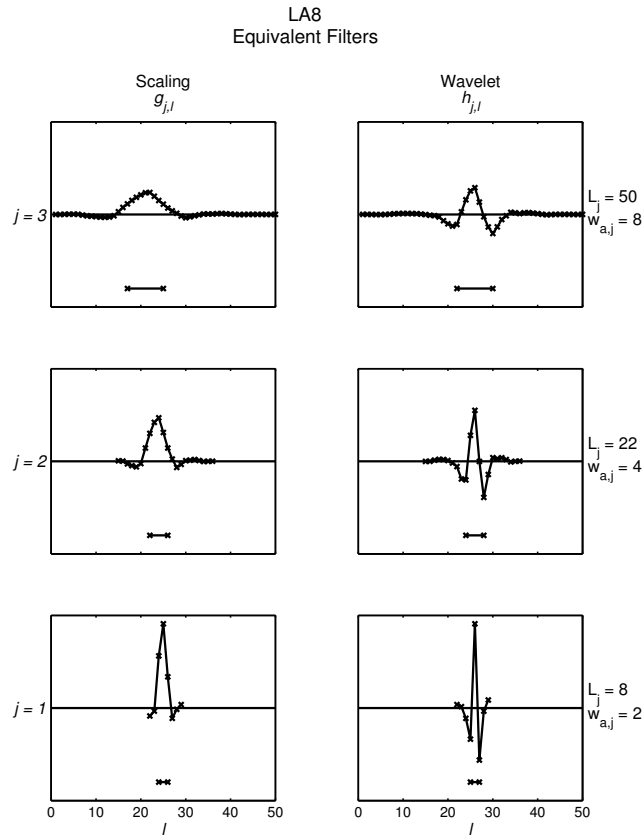


Figure 1. LA(8) scaling $\{\tilde{g}_{j,l}\}$ and wavelet $\{\tilde{h}_{j,l}\}$ equivalent filters for scales $j = 1-3$ aligned at filter midpoints. Horizontal line segment is the autocorrelation width $w_{a,j}$. Values of width of equivalent filter and autocorrelation width at each level are labeled to right.

Address for Offprints: Department of Atmospheric Sciences
 University of Washington
 Box 351640
 Seattle, WA 98195-1640, USA
 email: ccornish@atmos.washington.edu
 Fax: 206-685-9302

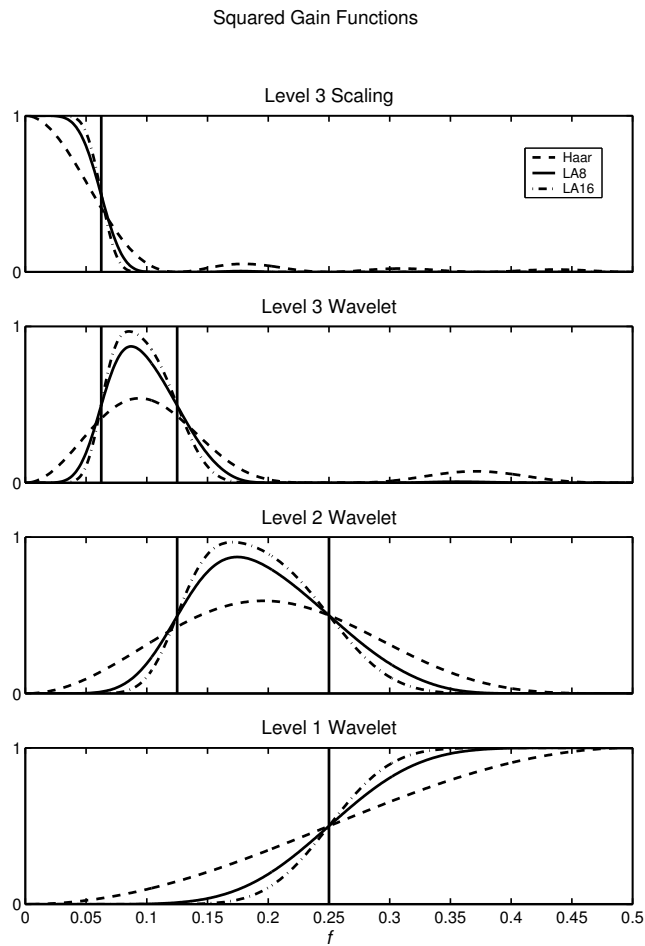


Figure 2. Squared gain functions of Haar (dashed), LA(8) (solid) and LA(16) (dash-dotted) filters for level 1-3 wavelet and third level scaling equivalent filters showing the band pass nature of the MODWT transform. Vertical lines delineate the nominal pass-bands.

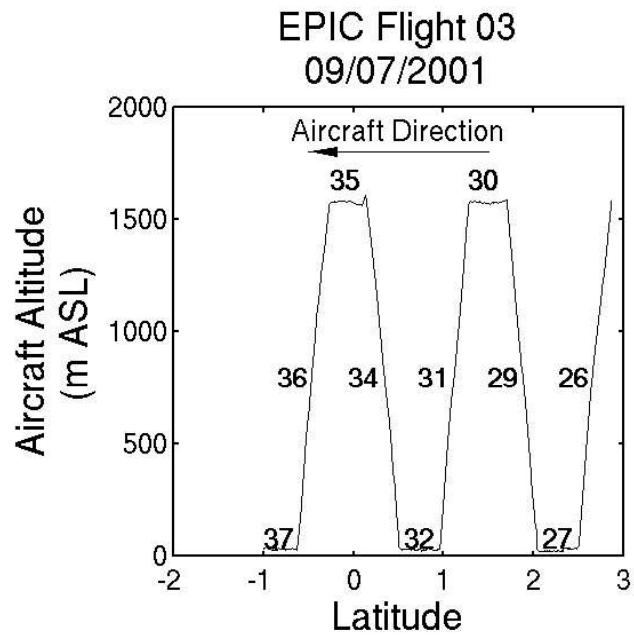


Figure 3. Aircraft altitude profile for portion of flight RF03.

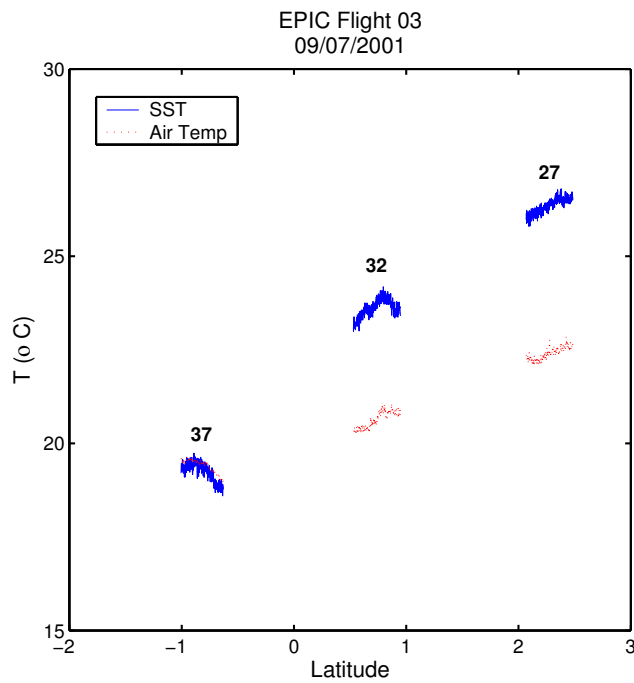


Figure 4. Observed sea surface and near surface air temperatures for three low level legs during flight RF03.

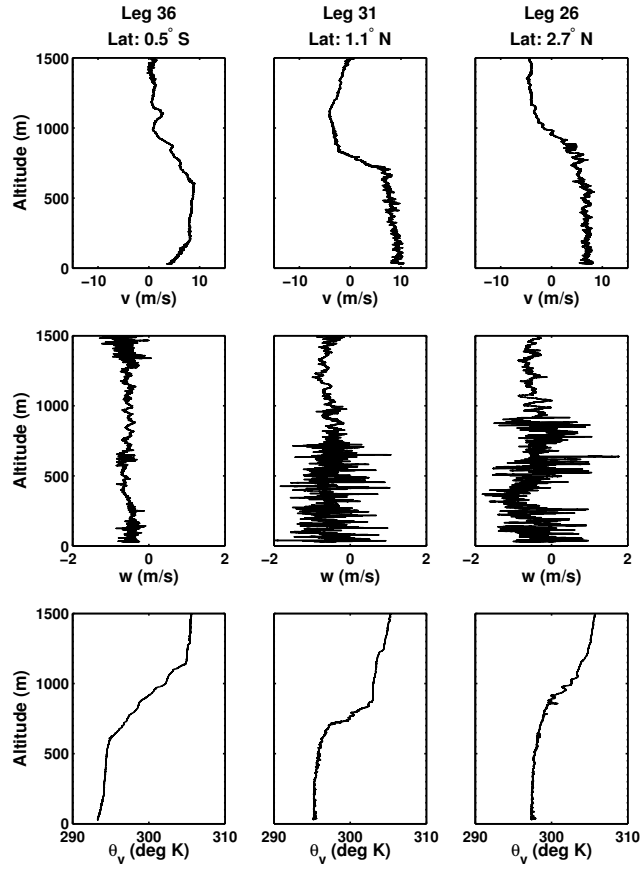


Figure 5. Profiles of meridional velocity (v , top row), vertical velocity (w , middle row) and virtual potential temperature (θ_v , bottom row) for three different latitudes near the equator. Profiles in leftmost column are over the cold SST ocean; profiles in rightmost column over the warm SST ocean.

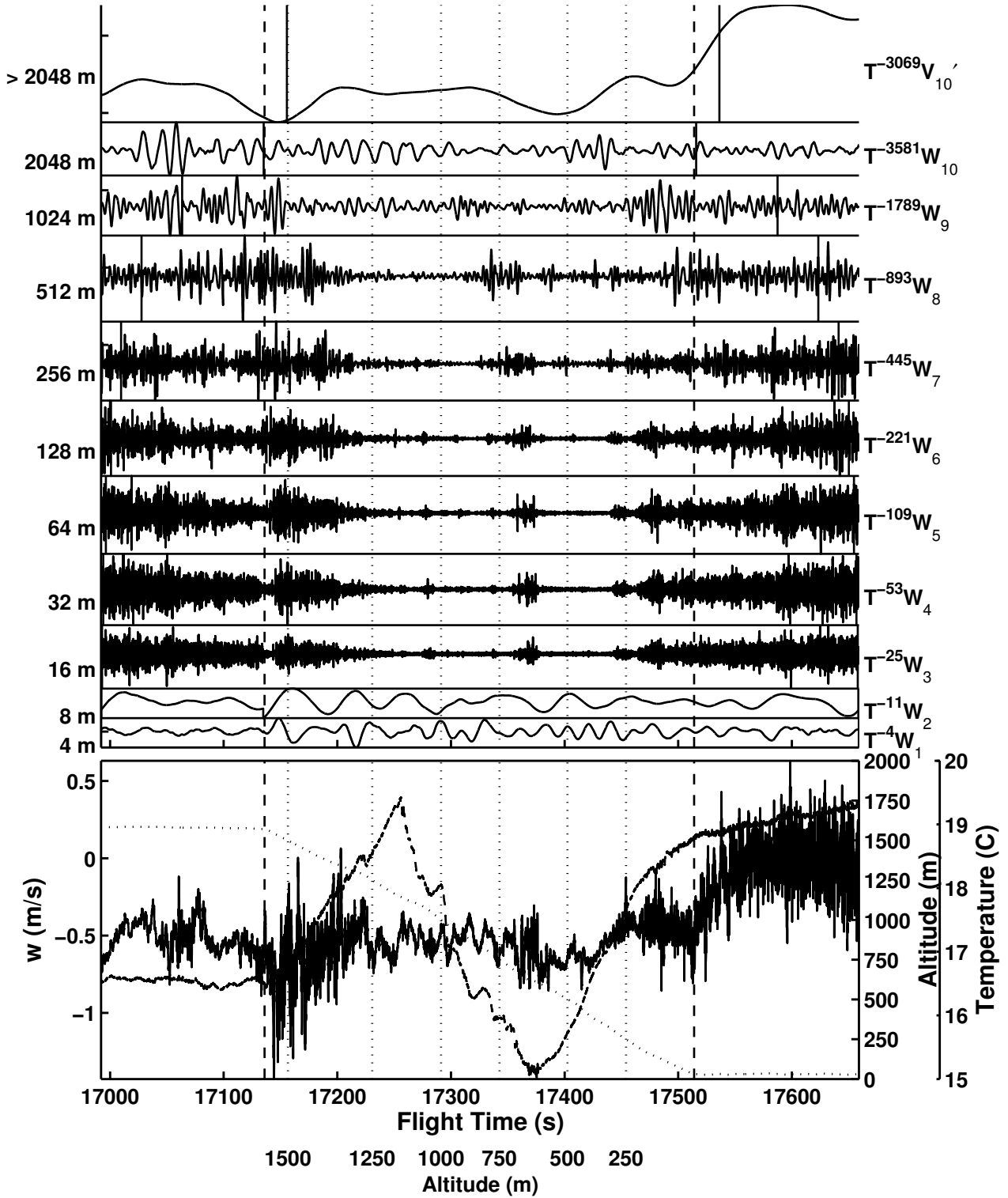


Figure 6. MODWT wavelet (levels 1–10) and scaling ($J_0 = 10$) coefficients (top panel) and original time series (bottom panel) of vertical velocity for leg 36 descent profile. Aircraft altitude (dotted curve) and ambient air temperature (dashed curve) are overlaid on time series. Vertical dotted lines show aircraft altitude at 250m intervals. Vertical dashed lines show start and stop times of descent profile. Solid vertical lines (top panel) indicate the boundaries outside of which coefficients are influenced by circular shifting. These are only discernible starting at level $j = 5$.

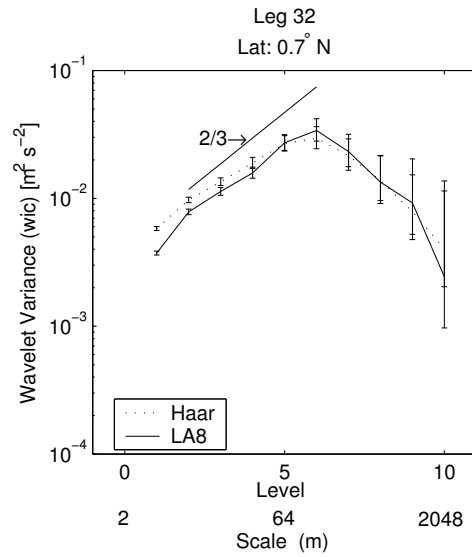


Figure 7. Unbiased wavelet variance estimates of vertical velocity (w) for low leg 32 computed using LA(8) (solid curve) and Haar (dotted curve) filters. Error bars indicate the 95% confidence intervals. Reference line with 2/3 slope represents expected shape for inertial subrange.

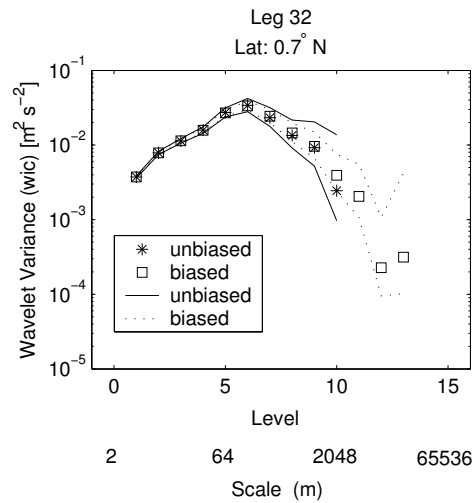


Figure 8. Wavelet variance (symbols) and confidence intervals (curves) of vertical velocity (w) for low leg 32 computed using LA(8) filter and two different estimators. Estimates are in good agreement for both estimators except at scale $j = 10$, for which the unbiased estimate is noticeably lower. Confidence intervals are tighter for the biased estimator than for the unbiased estimator, particularly for large j . The biased estimator provides values at larger scales because it makes use of all available coefficients.

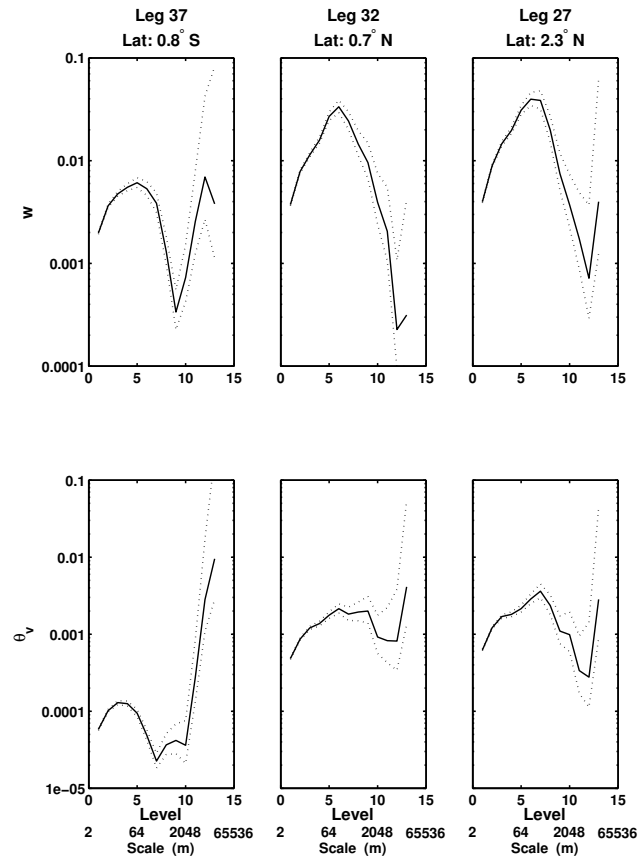


Figure 9. Biased wavelet variance (solid curve) of vertical velocity (w) and virtual potential temperature (θ_v) near the surface ($\sim 30\text{m}$) for three low flight legs at different latitudes near the equator. Dotted curves are the 95% confidence intervals. Vertical velocity wavelet variance is enhanced in regions warmer SST and increasing convective activity.

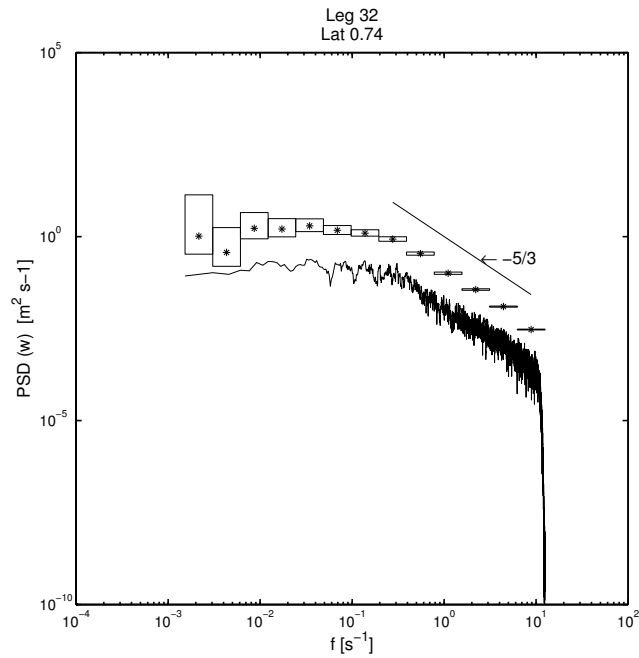


Figure 10. Power spectra of vertical velocities observed during low leg 32 calculated via Fourier multitaper method (bottom curve) and wavelet method using LA(8) filter (*) plotted using factor of 10 offsets. Line with $-5/3$ slope references Kolmogorov spectral shape for isotropic turbulence in the inertial subrange. Boxes indicate the confidence intervals for wavelet spectra for each pass-band.

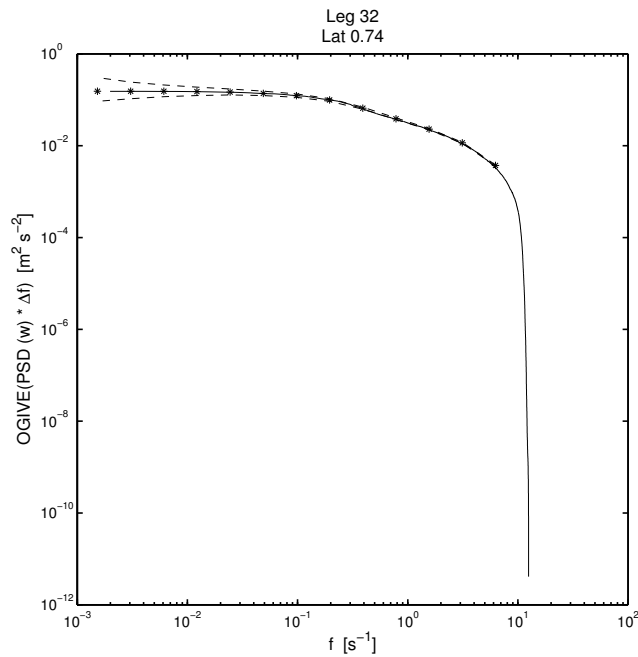


Figure 11. Ogive curves of cumulative power spectra for vertical velocity for leg 32 via Fourier multitaper (solid curve) and LA(8) wavelet (*) methods. Dashed curves are confidence bounds for wavelet method.

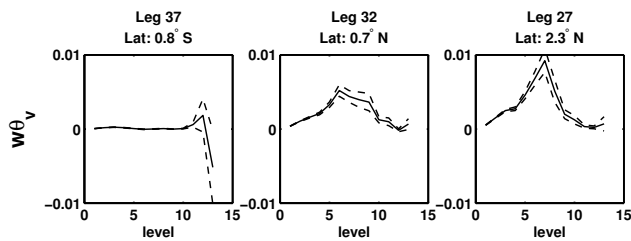


Figure 12. Biased wavelet covariance estimates (solid curve) and confidence intervals (dashed curves) of the vertical velocity (w) and virtual potential temperature (θ_v) near the surface ($\sim 30\text{m}$) for three low flight legs at different latitudes near the equator.

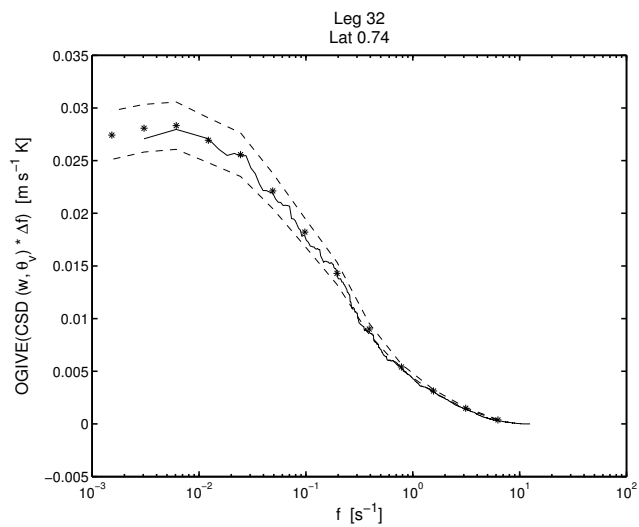


Figure 13. Ogive curves of cumulative cospectra for vertical velocity and virtual potential temperature for leg 32 via Fourier multitaper (solid curve) and LA(8) wavelet (*) methods. Dashed curves are confidence bounds for wavelet method.

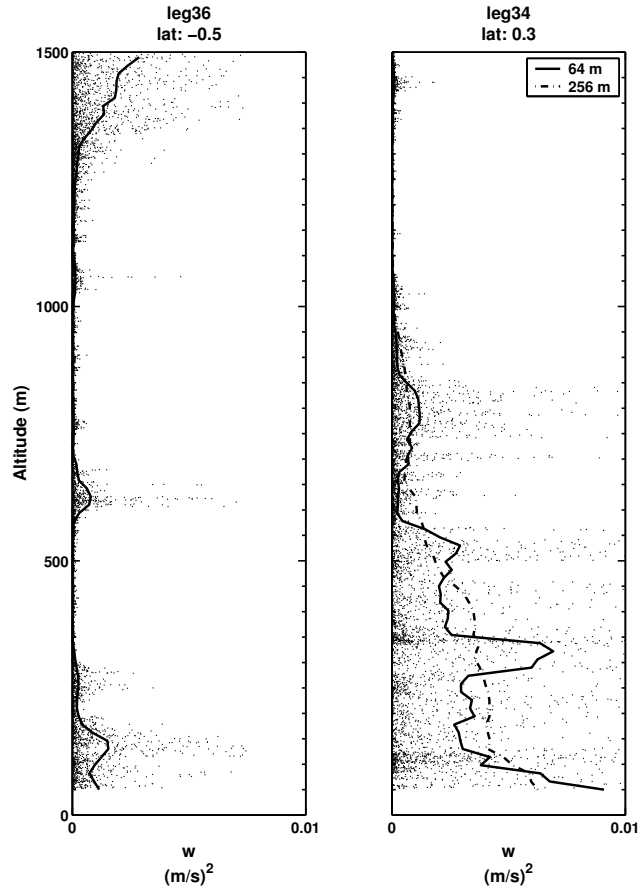


Figure 14. Running vertical velocity wavelet variance profiles for $j = 2$ level for legs 36 (cold SST) and leg 34 (warm SST). Points indicate squares of individual wavelet coefficients. Solid and dot-dash curves, respectively, show 400 (64 m) and 1600 (246 m) running averages of wavelet variance re-sampled at 16 m intervals.

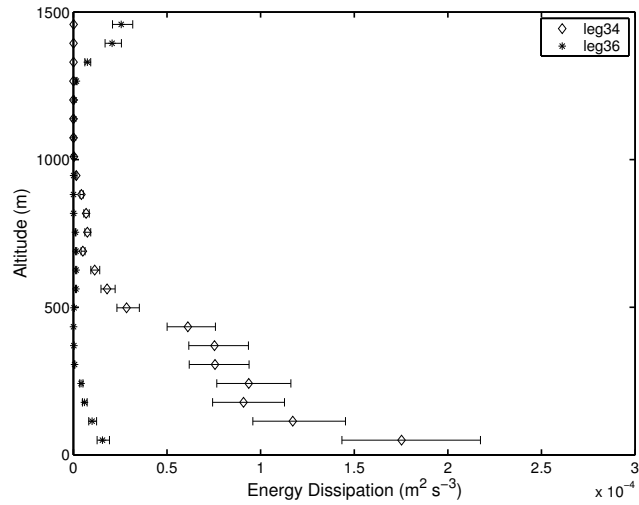


Figure 15. Profiles of energy dissipation with 95% confidence intervals derived using power spectra estimates from the level $j = 2$ wavelet variance. Values are computed from averages of 1600 adjacent coefficients corresponding to a height interval of 64 m. The dissipation of turbulent energy is significantly greater in the lower altitudes over the warm SST region (leg 36 labeled with asterisk) compared to the cold SST region (leg 34 labeled with diamond).

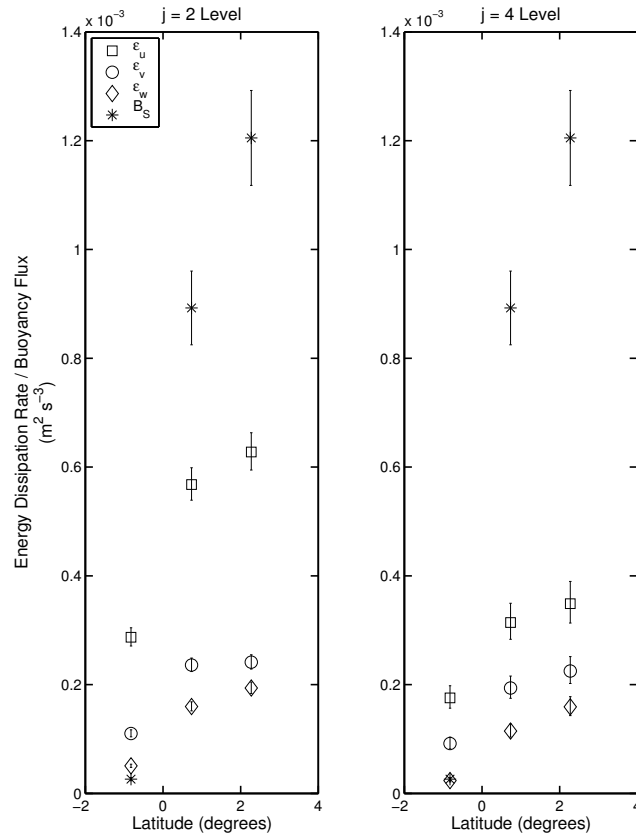


Figure 16. Buoyancy flux (B_S) derived from wavelet covariance and energy dissipation rates (ϵ) deduced from components of wavelet velocity power spectrum in surface layer for legs 37, 32, and 27. Estimates of ϵ are calculated from the $j = 2$ (left panel) and $j = 4$ (right panel) wavelet variance.

